High-Performance Cesium Ionizers Made from Sized Spherical Tungsten Powder

M. LaChance,* G. Kuskevics,† and B. Thompson‡
Electro-Optical Systems, Inc., Pasadena, Calif.

Sized tungsten microspheres of ~3-, 5-, and 7-μ mean diameter were used to fabricate cesium ionizers having improved uniformity, pore character, and ionization performance. With particle size the only intended variable, a gradient series of 80%-dense porous structures was prepared. Fabrication procedures plus data on sintering rates, densities, permeability coefficients, mean pore sizes, pores/cm^2, spectrographic purity, and cesium ionization performance are presented. Cesium ion current densities to 60 mÅ/cm^2 were achieved with 3- and 5-μ powder ionizers. Neutral fraction at 50 mÅ/cm^2 was 1–3%, considerable improvement over commercial tungsten and unsized spherical powder ionizers. Critical temperature was below Langmuir data for solid tungsten. Neutral fraction vs ionizer temperature curves for the 3-μ experimental ionizers showed definite minima and approximated slopes predicted by the Saha-Langmuir equation for work function 4.6–4.8 ev. Neutral fraction and critical temperature decreased with pore size for these structures. Photomicrographs confirm that use of 3-μ particles increased pores per unit ionizing area 5.5× and reduced mean pore size 0.4× (compared with use of coarse unsized microspheres). The fine spherical powder ionizers reached much higher current densities with lower neutral fractions than any other tungsten ionizers tested.

1. Introduction

CESIUM ion engines of the surface ionization type use a porous tungsten ionizer structure. It has been generally accepted that this ionizer structure should have as fine a pore size, with as many pores per unit area, as possible. Pore sizes and spacings from one to a few microns have been used. From physical considerations, it appears logical that pore size and distribution density be as uniform as possible. Furthermore, the ionizer structures and dimensions should not change significantly in thousands of hours at ionization temperature. The use of spherical, rather than hydrogen-reduced, tungsten powder was suggested by the relative metallurgical advantages of the spherical form. These advantages include high density of individual particles for transmitting compacting energy; smooth sphericity of particles for good packing uniformity prior to, and during, compaction; uniformity of strain energy at particle-contact points within the powder mass, as this relates to uniform densification in sintering; and minimum total surface free energy of spheres for relatively slow and controllable sintering to target density.

Fabrication procedures, structural characterization, and ionization performance are included in this paper. The only parameter, intentionally varied in fabrication, was the average size and size distribution of the spherical powder. Maintained as constant as possible were powder purity, compacting pressure, sintered density, infiltration procedures, removal of infiltrant, and final brazing into an ionization test fixture. This has permitted correlation of particle size and distribution with pore structures and, in turn, with ionization performance.

Presented as Preprint 64-692 at the AIAA Fourth Electric Propulsion Conference, Philadelphia, Pa., August 31–September 2, 1964; revision received April 5, 1965. This work was performed under NASA Contract No. NAS3-2519 at Electro-Optical Systems, Inc., Pasadena, Calif., and reported in Ref. 10. For assistance in the performance of this work, the authors wish to express their appreciation to A. Anglin and D. Lockwood of NASA Lewis; N. Winslow of Prado Laboratories, Cleveland, Ohio; H. Todd and R. Walker of Electro-Optical Systems (EOS); the Linde Research Laboratories of Indianapolis; and the Sharples Corporation of Bridgeport, Pa.

* Senior Metallurgist.
† Senior Scientist. Associate Fellow Member AIAA.
‡ Physicist.

2. Sizing and Size Analysis of Powder

A special fine grade of spherical tungsten powder was developed for this research program by the Linde Company. Spectrographic purity of the powder exceeded 99.94 wt %. The powder was sized in a Sharples K8 classifier, which separates powder in a dry condition, utilizing the drag force of a controlled air vortex. Wet methods of separation were unsuccessful because of a pronounced tendency of the microspheres to agglomerate. The various size fractions of powder were analyzed in the dry state by Micromerograph. This apparatus consists mainly of a powder deagglomerating device, a free-fall sedimentation column, and an electronic weighing balance and recorder. Particle size analysis by wet methods was precluded, as in sizing, by particle agglomeration.

Micromerograph size analyses are listed in Table 1. Here it is seen that classification 1) concentrated large percentages of particles within relatively narrow size ranges, and 2) removed essentially all particles below sharply defined minimum diameters. Predominant particle frequencies are defined by italics in Table 1.

3. Hydrostatic Pressing and Vacuum Sintering

All powders were pressed hydrostatically under 59,000 psi at room temperature and subsequently vacuum sintered at 1800° to 2200°C for 60 to 90 min under 10^{-5} to 10^{-6} torr pressure. Repeated attempts to prepare crack-free compacts by mechanical pressing (in a conventional cylindrical steel die) were unsuccessful. Two factors are believed responsible for such cracking, namely, the relatively low bond strength of pressed tungsten microspheres and the elastic recovery of the die walls on removal of ram pressure. Crack-free compacts were prepared by pressing the powders in Silastic rubber molds, inserted in a steel die. This arrangement permitted the mold walls to move away from, rather than toward, the compact upon decompression. It also permitted several compacts to be pressed simultaneously under uniform conditions.

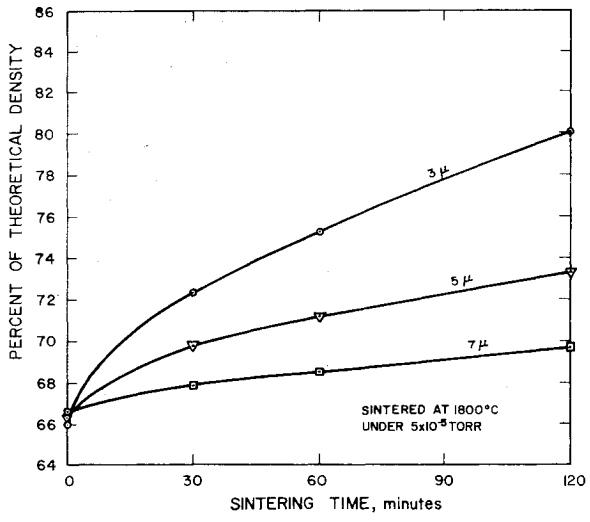

Fig. 1 Densification curves for three size fractions of spherical tungsten powder (rectangular compacts of ~4 cm³ volume, pressed isostatically at 59,000 psi).

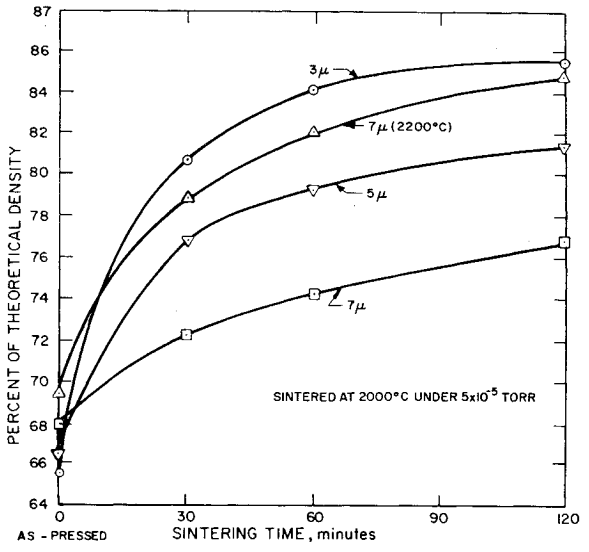

Fig. 2 Densification curves for three size fractions of spherical tungsten powder (rectangular compacts of ~4 cm³ volume, pressed isostatically at 59,000 psi).

To determine the sintering conditions necessary to achieve a target density of 80% theoretical, preliminary compacts were sintered at 1800°, 2000°, and 2200°C for 30-, 30-, and 60-min intervals. Densification rate curves are plotted in Figs. 1 and 2. These indicate normally that the finer the size (distribution) of the powder fraction, the more rapid the sintering rate. Thus, different size fractions require the use of different sintering schedules. Based on interpolation of Figs. 1 and 2, sintering conditions were selected which (in conjunction with final distillation heating) resulted in a common density of 80% of theoretical (see Table 2).

4. Infiltration, Machining, and Infiltrant Removal

To facilitate the machining of ionizer disks and to reduce associated surface deformation and pore closure, the sintered compacts were infiltrated by immersion in Cu-2wt % Fe alloy at 1175°C for 30 min under hydrogen atmosphere. Ionizer disks $\frac{3}{16}$ in. in diameter × 0.04 in. thick were machined and subsequently surfaced under controlled conditions. Three different surfaces were applied by lathe turning, wet machine grinding, and metallographic polishing. Average peak-to-valley contours obtained were 60 μin., 6.5 μin., and < 1 μin., respectively. The infiltrant was removed subsequently by heating in vacuum at 1500°C for 15 min and finally at 1750°C for 45 min. These conditions were chosen for most efficient removal of the infiltrant, consistent with raising the density to, but not exceeding, the 80% target. Spectrographic purity of all ionizer disks exceeded 99.92 wt%.

Table 1 Particle size distribution of powder fractions used to prepare ionizers

Particle diam range, μ	3μ		5μ		7μ	
	Wt %	No. %	Wt %	No. %	Wt %	No. %
0–1	nil	nil	nil	nil	nil	nil
1–2	2.8	*25.2*	nil	nil	nil	nil
2–3	22.4	*43.6*	nil	nil	nil	nil
3–4	28.0	*19.9*	8.0	*25.3*	nil	nil
4–5	23.3	7.8	23.3	*34.6*	2.2	*13.7*
5–6	14.0	2.6	29.7	*24.2*	8.3	*28.3*
6–7	7.7	0.9	22.3	11.0	12.0	*24.8*
7–8	1.8	0.1	11.9	3.8	10.4	*14.0*
8–9	nil	nil	4.8	1.1	8.0	7.4
9–10	nil	nil	nil	nil	6.1	4.0
10–11	nil	nil	nil	nil	4.5	2.2
11–12	nil	nil	nil	nil	3.6	1.3
12–13	nil	nil	nil	nil	3.2	0.9
13–14	nil	nil	nil	nil	3.1	0.7
14–15	nil	nil	nil	nil	3.2	0.6
15–20	nil	nil	nil	nil	13.6	1.5
20–25	nil	nil	nil	nil	10.4	0.5
25–30	nil	nil	nil	nil	6.4	<0.1
30–40	nil	nil	nil	nil	5.0	<0.1

5. Characterization of Pore Structure

Since the permeability of a porous body is very sensitive to slight differences in pore structure, the permeability coefficients of all experimental ionizer disks were determined. The permeability apparatus used is shown in Fig. 3. A sample disk is clamped in the test fixture within a rubber O-ring to seal the sample edges, such that only the flat face area is exposed to the gas flow. Other components of the apparatus consist of a nitrogen tank, drying tower, solenoid gas valve, mercury manometer, and gas chamber of known volume. Nitrogen pressure between tank and solenoid valve is adjusted first so that, when the valve is energized, 1) mercury in the manometer rises to above the upper electrical contact in the manometer, 2) nitrogen is admitted to the gas chamber, and 3) diffusion of nitrogen is initiated through the porous sample. As mercury in the manometer falls below the upper electrical contact, the stop clock is actuated electrically and continues to run until the mercury breaks from the lower contact (located 40 mm below the upper one). The time interval δt obtained in this way can be read to the near-

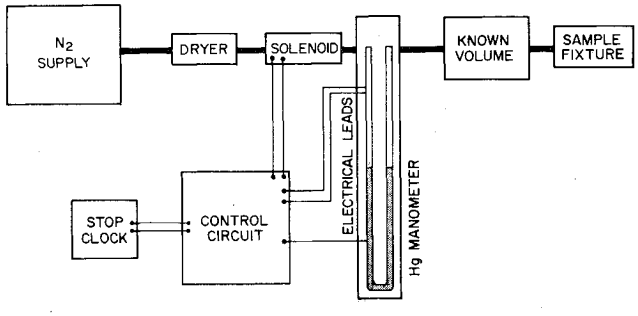

Fig. 3 Block diagram of permeability apparatus.

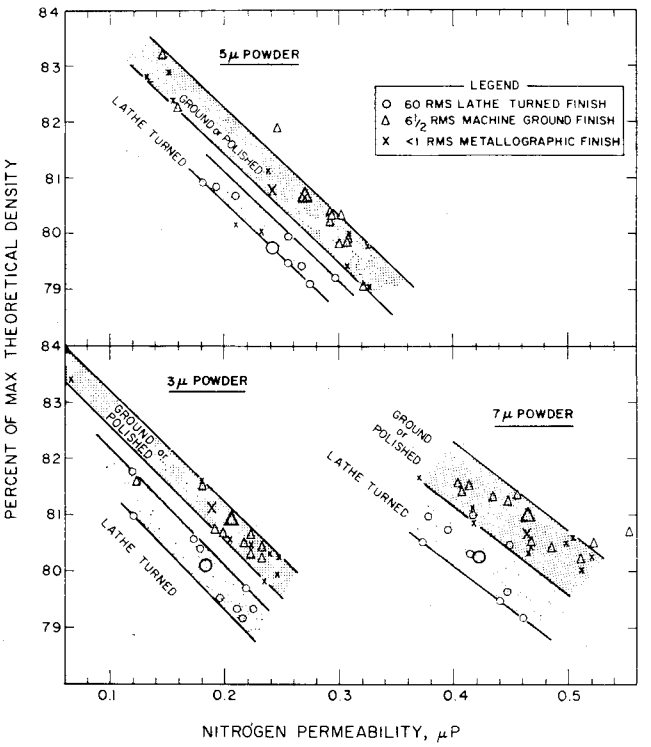

Fig. 4 Density vs nitrogen permeability for ionizer disks, made from 3-, 5-, and 7-μ tungsten microspheres, showing the effect of surface finish.

est 0.01 sec. Several readings are made on each ionizer to stabilize moisture content and to obtain valid δt averages.

Mass permeability coefficient is calculated by Carman's formula[1]:

$$K = \delta m \frac{L}{A} \frac{1}{\delta t} \frac{1}{\Delta P}, \text{ g}\cdot\text{cm}^{-1}\cdot\text{sec}^{-1}\cdot\text{torr}^{-1}$$

where

δm = $\delta P \cdot V \cdot M/R \cdot T$, g
δP = small finite pressure decrement, atm
V = gas volume, cm^3
M = molecular wt of gas, g/mole
ΔP = mean differential pressure between chamber and atmospheric during δp decrement
R = ideal gas constant
T = absolute temperature, °K
L/A = disk thickness/circular area, cm^{-1}
δt = time for δP decrement, sec

In subsequent discussion, K will be referred to as nitrogen permeability, with $10^{-6}\cdot\text{g}\cdot\text{cm}^{-1}\cdot\text{sec}^{-1}\cdot\text{torr}^{-1}$ designated as a microperm (μP).

The nitrogen permeabilities of the ionizer disks are plotted against their apparent densities in Fig. 4. Here the data points lie within distinct bands, with permeabilities increasing normally with decreasing densities. Data for wet machine ground and for metallographically polished ionizers are quite congruous (within each powder size category), indicating that these surfacing operations effect similar degrees of pore closure. Data bands for lathe-turned ionizers are offset consistently toward lower permeabilities, indicating significantly more pore closure. Based on these data, all ionization testing, reported subsequently in this paper, was performed on disks surfaced by wet machine grinding.

Whereas apparent densities and permeability coefficients are direct indicators of bulk porosity, they tell nothing of pore size. Techniques for determining pore size include mercury intrusion, specific area measurement, and calculation from pore counts. Mercury intrusion and pore-count data were obtained on the experimental spherical powder ionizers. An Aminco-Winslow Porosimeter was used for the former. This apparatus consists mainly of a pump to evacuate the porous sample, a mercury pressurizing piston, and a penetrometer to measure accurately the mercury absorbed.[2] After evacuation of air from the pores, mercury was intruded under pressures up to $\approx$5000 psi, and the cumulative volumes absorbed were measured at specific pressure levels. Where pore structure is of simple capillary configuration, correlation of mercury pressure with intruded pore diameter may be obtained by the Dupré equation[3]:

$$D = -4\epsilon \cos\theta/P$$

where ϵ is the surface tension of Hg, and θ is the wetting angle between Hg and test sample. However, the fine structure of the experimental sintered ionizers is not of the simple capillary type; rather, it consists of an interconnected network of channels of greatly variable cross section. Thus, what appears in a plane view as a large pore is actually a void space, connected to the maze structure by perhaps several restricted channels or necks. Treatment of the intrusion data as for capillary porosity can lead to interpreting a single large void as many small capillaries, having the diameter of the largest access channel. In turn, this will indicate a much finer pore size distribution than is observable directly from photomicrographs.

All mercury intrusion data obtained on sintered ionizers are listed in Table 3. These data indicate that occluded pore volumes are all less than 1% of the sample volumes. It is apparent also, from the "intrusion pressure vs absorbed volume" data, that the 3-μ spherical powder sample has the finest pore distribution (most restricted maze), the coarse unsized sample, the coarsest distribution (least-restricted maze), and that the other samples are intermediate, in the order listed. This trend correlates with that indicated by photomicrographs in Fig. 5 and with the data tabulated in Table 4.

In summary, data obtained on spherical powder ionizers at 80% density indicate that, as the size distribution of initial particles is decreased, 1) sintering rate increases, 2) volume of occluded pores increases slightly, 3) pore size and size distribution decrease, 4) number of pores per unit area increases, and 5) permeability coefficient decreases. These trends are in good agreement with the normal behavior of sintered metal powder.

6. Ionization Performance of Sized Spherical Tungsten Powder

The cesium ionization performance of sized spherical powder ionizers was obtained by measuring the neutral fraction and critical temperature as a function of ion current density and ionizer structure. The ionizer criteria, test apparatus, and measurement procedures have been described previously.[4] Minor modifications included better temperature control and measurement, use of continuous and x-y recorders for faster data evaluation, and a better (10^{-7} torr) vacuum system. The porous tungsten ionizers were vacuum brazed into molybdenum holders. Active ion emission area was subsequently measured by the diode sputtering pattern method.[4] Experimental procedures are described in more detail in Ref. 5.

Cesium Permeability

Since the neutral fraction of all spherical powder ionizers is only a few percent at the most, the total cesium ion current density can be taken as a measure of cesium permeability. When the ion current density is plotted on a logarithmic scale against the cesium reservoir temperature on a $1/T$ scale, the resulting graphs are straight lines. Spherical

Table 2 Sintering conditions for ionizers

Powder fraction	Sintering		Est'd sint. density, %	Est'd den. after[a] dist'n of infiltrant	Actual den.[b] after dist'n
	Temp., °C	Time, min			
3μ	1800	60	75.3	79.0	80.7
5μ	1900	90	77.8	79.3	80.5
7μ	2100	70	78.6	79.6	80.7

[a] Vacuum distilled at 1500°C for 15 min plus 1750°C for 45 min.
[b] Average values based on 29 ionizer disks.

powder ionizers, made from various powder size fractions, had a narrow distribution of cesium permeabilities. The commercial hydrogen-reduced powder ionizers have a slightly lower cesium permeability and larger spread. Wire bundle ionizers generally had much higher permeability and even larger spread. To correlate cesium permeability at the ionization temperature with nitrogen permeability at room temperature, Fig. 6 was prepared from ion current density vs reservoir temperature, by taking direct or extrapolated points at 300°C. The limited number of points leads to the following conclusions:

1) There appears to be a linear correlation of cesium and nitrogen permeability for a given structure of a given pore size. This is evidenced by the 45° slope.

2) For a given structure, the cesium permeability increases with decreasing pore size (increasing number of pores per unit area) for a constant nitrogen permeability.

Since the pore diameter is about 50× the mean free path for nitrogen at room temperature and atmospheric pressure, the nitrogen flow could be in the transition region. One would expect no flow by surface diffusion. The cesium vapor flow, at ionizer temperature and with the few mm Hg pressure on one side, is expected to be in molecular flow with a surface diffusion component. At a constant pressure and temperature, viscous flow is proportional to the fourth power of the pore diameter, molecular flow to the third power, and surface diffusion flow to the first power of the pore diameter. Plotting the cesium permeability vs the pore diameter would give information about the nature of the flow. There is considerable scatter of the small number of points. Also, uncertainty is introduced by using the total prebraze geometrical area for calculating the nitrogen permeability and the measured active ion emission area for calculating the cesium permeability. An attempt to correlate flow rate with pore size was postponed until more data become available. If the difference between nitrogen and cesium permeability was due to the viscous flow component of nitrogen at room temperature and atmospheric pressure, then the nitrogen flow through the fine pore ionizers should be larger than the cesium flow, or a trend in the opposite direction from the present would be expected. The higher cesium permeability for the fine pore ionizer samples thus could be due only to the additional permeability due to surface diffusion. The active area for spherical and angular powder ionizers is approximately 12% smaller than the total before-brazing ionizer area, and the effective area for nitrogen conductance after brazing is about 40 to 50% smaller than the total button area. The actual numbers for the series of ionizers tested are given in Table 5, with the effective cross section area for nitrogen conductance being obtained from the ratio of the nitrogen permeability after brazing to the nitrogen permeability before brazing. A more accurate check on the dependence of cesium permeability on ionizer temperature was performed by adding the ion current and equivalent neutral current to verify the approximately 3%/100°C decrease in cesium permeability vs temperature.

7. Upper and Lower Critical Temperatures for Solid and Porous Tungsten

Ionization performance of the series of sized spherical powder ionizers was obtained by measurement of the ion current and neutral fraction vs the ionizer temperature for a set of different cesium flow rates. Most data for solid tungsten, as measured by Langmuir,[6] was obtained by increasing the temperature and measuring the more reproducible upper critical temperature, as shown in Fig. 7. Most of the ionizer performance measurements are done by decreasing the ion-

Table 3 Density, pore volume, and mercury intrusion data for sintered tungsten ionizers

Powder type	3-μ spherical		5-μ spherical		7-μ spherical		H_2-reduced,[a] coarse		Spherical coarse, unsized	
Avg. particle diam, μ	2.72		4.87		6.92		(?)		3.47	
Vol. of sample, V_s, cm³	0.32509, cm³		0.34798, cm³		0.37099, cm³		0.35076, cm³		0.36275, cm³	
Final density, % of theor.	79.63		80.31		80.73		81.50		79.02	
Total pore vol., % of V_s	20.37		19.69		19.27		18.50		20.98	
Open pore vol., % of V_s	19.70		19.25		18.87		17.53		20.68	
Occluded pore vol., % of V_s	0.67		0.44		0.40		0.97		0.30	
	Volumes of mercury intruded over respective pressure ranges									
Mercury pressure, psi	ΔV, cm³	% of V_s	ΔV, cm³	% of V_s	ΔV, cm³	% of V_s	ΔV, cm³	% of V_s	ΔV, cm³	% of V_s
43–55	nil	nil	nil	nil	nil	nil	nil	nil	0.001	0.28
55–73	nil	nil	nil	nil	nil	nil	0.002	0.57	0.052	14.33
73–102	nil	nil	0.001	0.29	0.001	0.27	0.054	15.39	0.018	4.96
102–160	0.001	0.31	0.037	10.63	0.064	17.25	0.004	1.14	0.003	0.83
160–235	0.055	16.92	0.026	7.47	0.004	1.08	0.001	0.29	0.001	0.28
235–335	0.006	1.85	0.002	0.57	nil	nil	nil	nil	nil	nil
335–568	0.001	0.31	nil	nil	nil	nil	nil	nil	nil	nil
568–1735	0.001	0.31	0.001	0.29	0.001	0.27	0.0005	0.14	nil	nil
	0.064	19.70	0.067	19.25	0.070	18.87	0.0615	17.53	0.075	20.68

[a] Purchased ionizer, reported to have the finest pore size sold in large pieces as of 11/63.

izer temperature. For the solid tungsten this would give the lower critical temperature, resulting in a curve as shown in Fig. 7. The upper critical temperature line of Fig. 7 was measured to 2 mÅ/cm², giving an empirical equation

$$\log_{10}\mu_a = 27.791 - 14350/T_C$$

Here μ_a is the rate of cesium atom incidence, in atoms/cm²-sec, which is equal to the rate of cesium ion evaporation. These data are not consistent with the upper critical temperature data calculated by Langmuir[7] from atom absorption data in Ref. 6, resulting in the equation

$$\log_{10}\mu_a = 25.66 - 11500/T_C$$

Since, with the porous ionizers, the lower temperature is measured, it can be obtained from the same atom desorption data and is very nearly represented by

$$\log_{10}\mu_a = 24.6549 - 10730/T_C$$

This equation, plotted in Fig. 8, agrees with experimental data for the lower critical temperature of solid tungsten.[9]

With the measurement of the neutral fraction for porous ionizers, there are sometimes two lower critical temperatures, one, T_{CI}, defined as the temperature at which ion current has declined by a minimum detectable amount, say 5%, and the other, $T_{C\alpha}$, defined as the temperature correspondent with the minimum neutral fraction (Fig. 9). The $T_{C\alpha}$ point may be close to the upper critical temperature. The higher the ion current density, and the cleaner the tungsten surface, the smaller the difference between the upper and lower critical temperature. The optimum ionizer operating temperature should lie in a relatively small range between the lower current critical temperature T_{CI} and the higher neutral critical temperature $T_{C\alpha}$.

Table 4 Data for tungsten ionizer structures of Fig. 5

Powder type	Density, % of theor.	N_2 perm., μP	Mean pore diam, μ	Den. of pore packing, pores/cm²
3μ	79.63	0.21	2.50	4.01×10^6
5μ	80.31	0.33	3.51	1.99×10^6
7μ	80.73	0.50	3.83	1.64×10^6
Coarse comm.	81.50	0.60	5.43	0.76×10^6
Coarse sph.	79.02	0.85	6.05	0.72×10^6

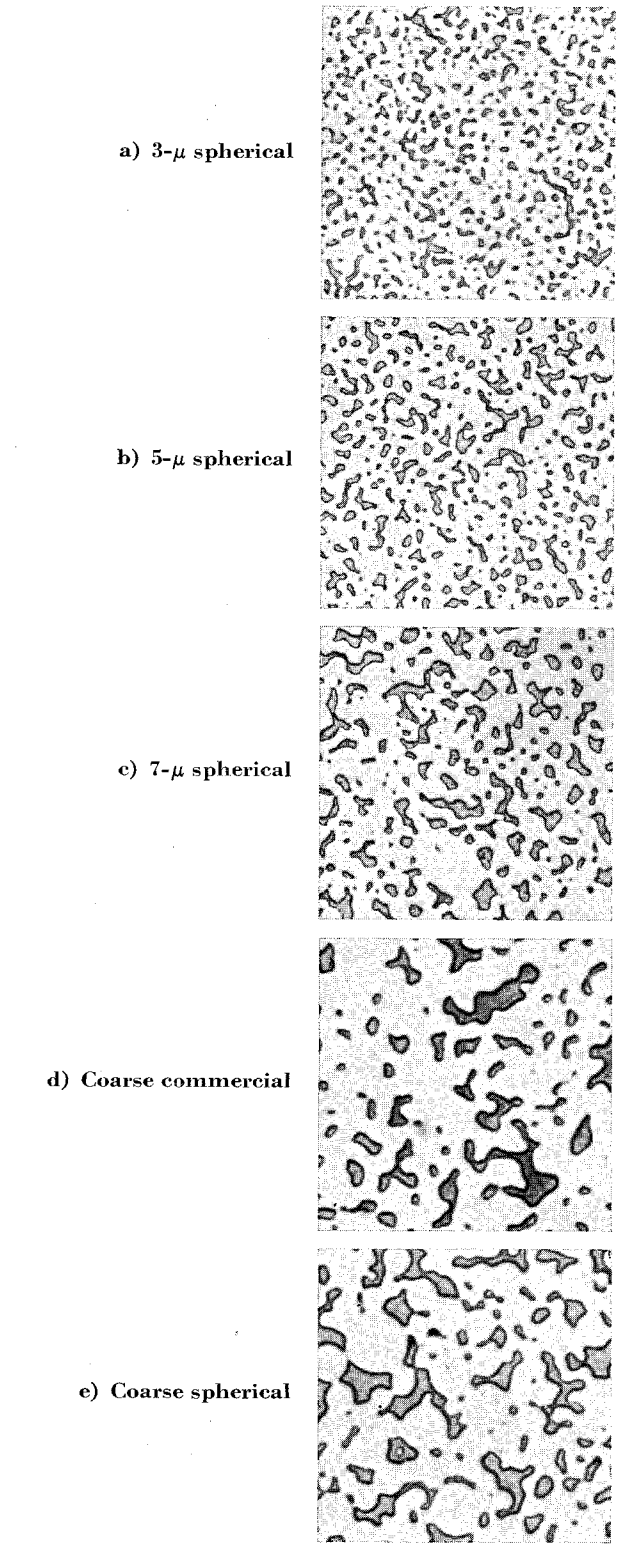

Fig. 5 Typical pore structure of tungsten ionizers made from various size fractions of powder (400×).

8. Comparison of Ionization of 3-, 5-, and 7-μ Spherical Tungsten Powder Ionizers

As evident from the photomicrographs in Fig. 5 and parameters such as average pore size, pores per cm², and pore size distribution, the 3-μ spherical powder ionizer structure has the most uniform and the finest structure produced to date. These 80% dense structures also have the lowest nitrogen permeability of spherical or commercial structures. Upon brazing, the 3-μ *SP* ionizers suffer the lowest reduction of

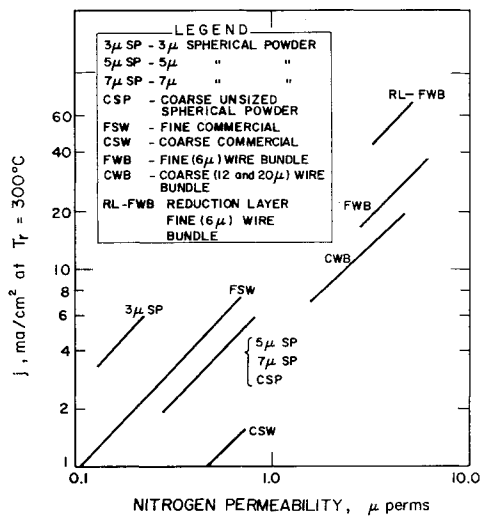

Fig. 6 Correlation of cesium and nitrogen permeability for spherical powder (*sp*), commercial (*sw*), and wire bundle (*wb*) ionizers. Data from *wb* extrapolated.

Table 5 Mechanical parameters of selected ionizers

Ionizer designation	3-μ *SP*	5-μ *SP*	7-μ *SP*	Coarse commercial tungsten
Powder type	3-μ spherical	5-μ spherical	7-μ spherical	H_2-reduced
Average particle size, μ	2.72	4.87	6.92	...[a]
Ionizer density, % theoretical	80.41	79.90	80.41	81.40
Thickness, cm	0.0937	0.0965	0.0968	0.1029
Total area, cm^2	0.169	0.176	0.177	0.178
Active area, cm^2	0.150	0.162	0.161	...
N_2 permeability, μP	0.232	0.308	0.485	0.592
N_2 permeability after brazing, μP	0.164	0.220	0.369	0.161
Mean pore diam, μ	2.50	3.51	3.83	5.43
Pores per cm^2	4.01×10^6	1.99×10^6	1.64×10^6	0.76×10

[a] Purchased material, powder size used unknown.

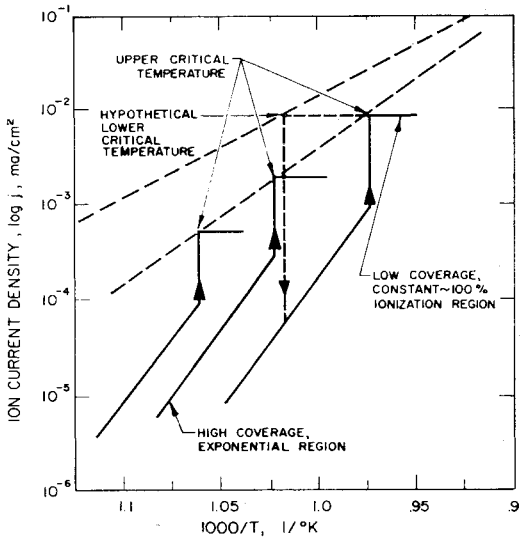

Fig. 7 Definitions of surface ionization regions for ion current-ionizer temperature curves for solid tungsten.

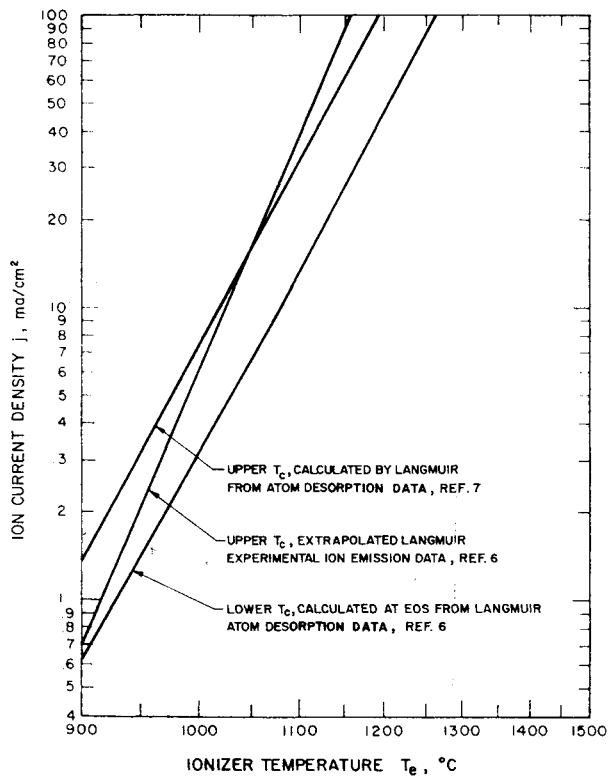

Fig. 8 Critical temperature curves for cesium ionization on solid tungsten.

nitrogen permeability (only 25 to 35%), which implies the lowest braze infiltration. Also as shown in Fig. 6, these ionizers have the highest cesium permeability compared to other ionizers of equal nitrogen permeability. The complete set of performance curves for a 3-μ spherical powder ionizer, shown in Fig. 10, represents the best ionizer material ever tested at Electro-Optical Systems. Note that the lower ion critical temperature is below the lower solid tungsten critical temperature in Fig. 10a. The curves shown were obtained on the second day of the experiment (first digit of legend). Sequence of testing is designated by the second digit of the legend. Corresponding neutral fraction curves are shown in Fig. 10b. The neutral fraction curves, at higher ionizer temperatures and low neutral fractions, start to follow the Saha-Langmuir slopes (shown in the plot) corresponding to tungsten work functions of between 4.6 and 4.8 ev. A plot, similar to the theoretical plots of Forrester and Speiser,[8] combines the ion current and neutral fraction data in Fig. 10c. These curves show that, if a given neutral fraction is desired, there is an optimum ion current density corresponding to a given ionizer temperature. However, one can operate at this same neutral fraction at a lower ionizer temperature if some ion current density can be sacrificed. The usual neutral fraction vs ion current density plot is shown in Fig. 10d going up to a maximum of 50 mÅ/cm^2. Similar results were obtained on two samples of the 3-μ spherical powder. The 5-μ spherical powder structure (see Fig. 5) had a larger pore size and a lower number of pores per cm^2. This ionizer was operated to 60 mÅ/cm^2 with only a 3% neutral fraction at that point. Similarly, the

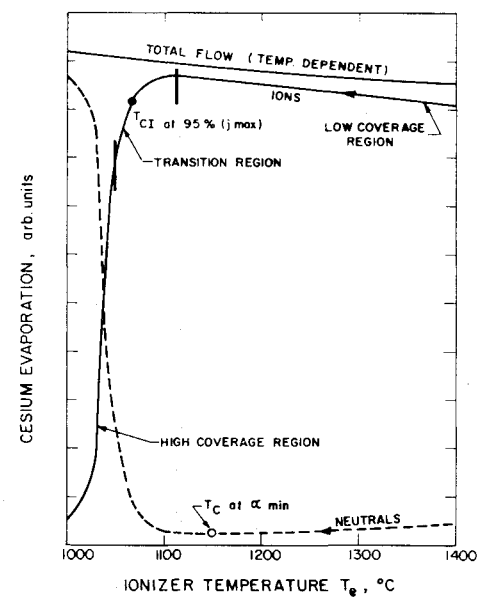

Fig. 9 Ion current, neutral efflux and total flow vs ionizer temperature for porous tungsten.

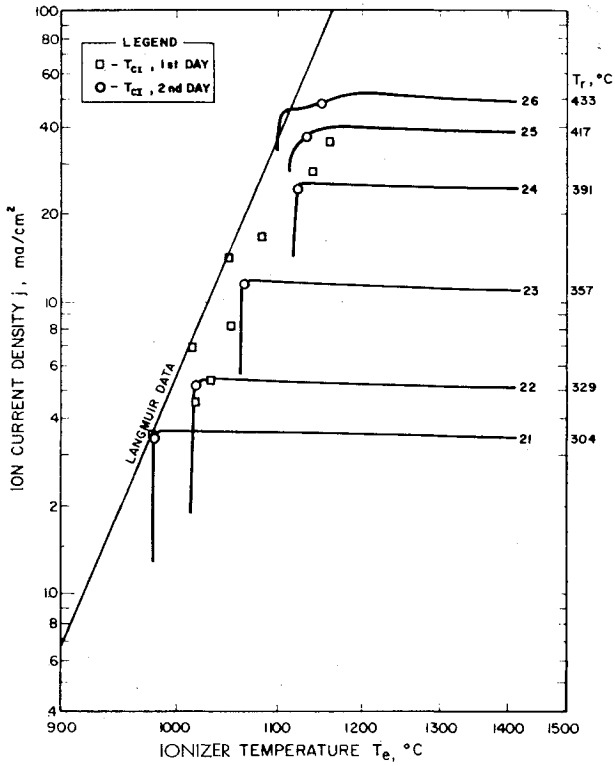

a)

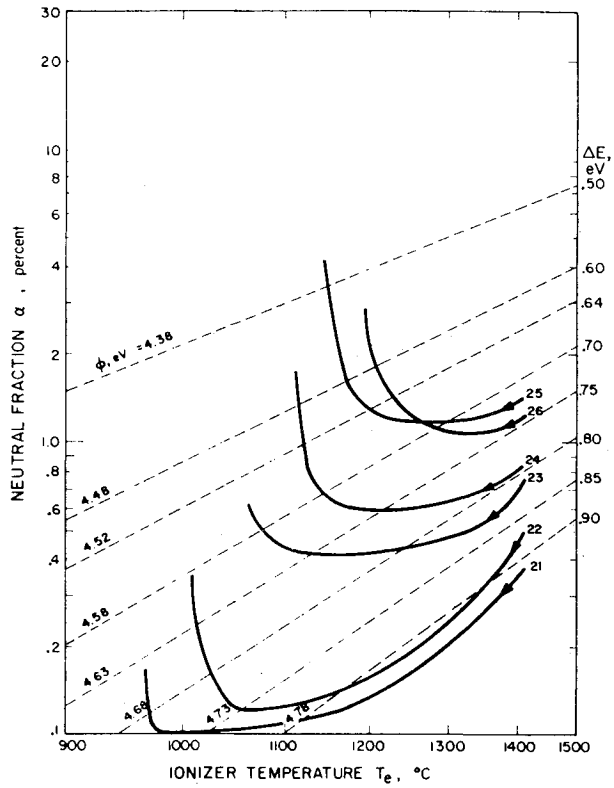

b)

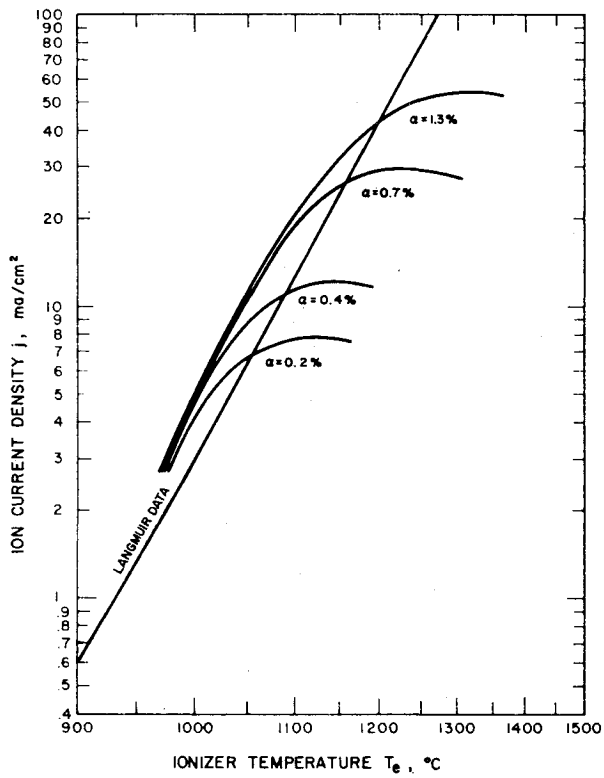

c)

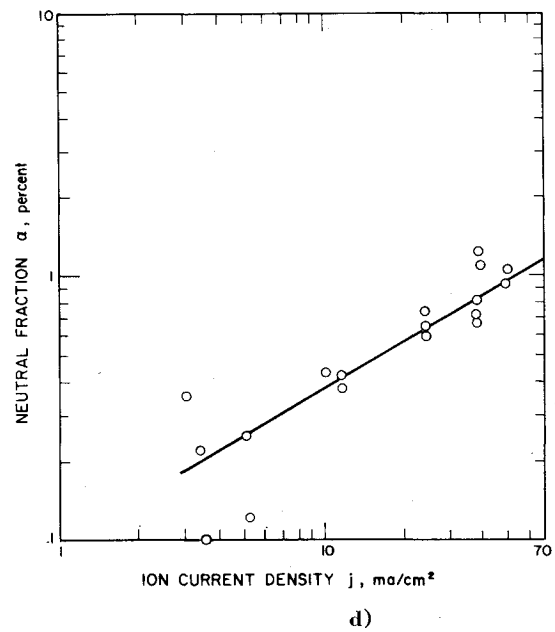

d)

Fig. 10 Performance curves for 3-μ spherical powder tungsten ionizer.

lower critical temperature obtained was 50° to 100°C lower than Langmuir data. Only one of these ionizers was tested. The 7-μ spherical powder ionizer had the largest nitrogen permeability even though the average pore diameter was only slightly higher than that for the 5-μ sample. With two samples tested, the highest current density was about 30 mÅ/cm². The best data obtained from these three structures are indicated in Fig. 11, together with comparison curves for unsized spherical powder, fine and coarse commercial ionizers, and fine and coarse wire bundle ionizers. It is

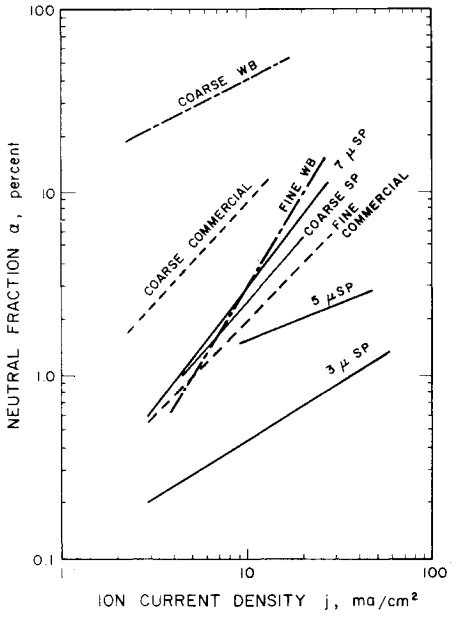

Fig. 11 Comparison of performance of coarse and fine size structures for three different structural types of tungsten.

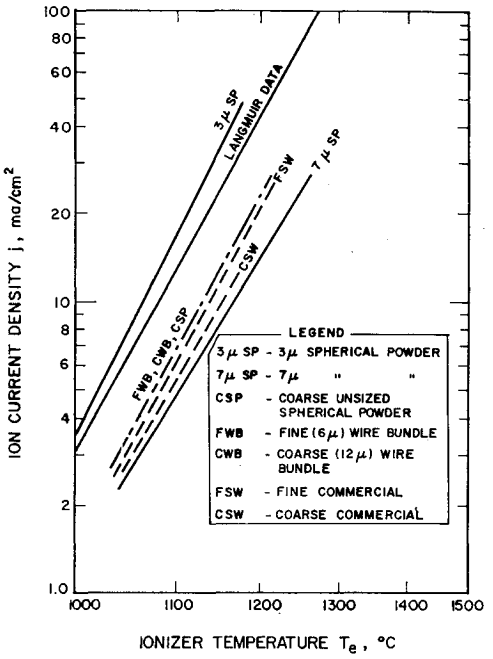

Fig. 12 Comparison of ion current-critical temperature of coarse and fine size structures for three different structural types of tungsten.

evident from Fig. 10c that the 3- and 5-μ sized spherical powder ionizers give the lowest neutral fractions at a given current density. A similar comparison of critical temperatures is indicated in Fig. 12 for the same ionizers.

9. Effect of Oxygen and of Oxidation Reduction

Starting with the background residual pressure of about 5×10^{-7} torr, oxygen was submitted to the test chamber to see if the ionization parameters changed with the increase in pressure. Based on preliminary tests, the critical temperature at first increased, reached a maximum, and subsequently decreased. The neutral fraction first decreased, reached a minimum at the same time as the critical temperature went through a maximum, and subsequently increased. This occurs during the pressure change of about $2\frac{1}{2}$ decades. The ionizer recovers from exposure to high pressure very slowly. An oxidation-reduction treatment was tried with fine wire bundle and spherical powder ionizer structures. This treatment resulted in reduction of the critical temperature but an increase in neutral fraction. The oxidation-reduction treatment is believed to provide extremely fine pores at the surface of the ionizer, though such refinement has not been verified metallographically.

References

[1] Carman, P. C., *Flow of Gases Through Porous Media* (Butterworths Scientific Publications, Ltd., London, 1949).

[2] Winslow, N. M. and Shapiro, J. J., "An instrument for the measurement of pore-size distribution by mercury penetration," Am. Soc. Testing Materials Bull. 236, 39 (February 1959).

[3] Holdsworth, S. D., "Characterization of porous materials," Chem. Process Eng. **44**, 184 (April 1963).

[4] Kuskevics, G. and Thompson, B. L., "Comparison of commercial, spherical powder and wire bundle tungsten ionizers," AIAA J. **2**, 284–294 (1964).

[5] Kuskevics, G. and Teem, J. M., "Ionization and transport phenomena and performance of porous ionizers," *Symposium on Physics and Technology of Ion Motors, 13th General Assembly* (Gordon and Breach Science Publishers, Inc., New York, 1965); also Electro-Optical Systems, Inc. EOS Research Rept. 16 (September 1963).

[6] Taylor, J. B. and Langmuir, I., "The evaporation of atoms, ions, and electrons from cesium films on tungsten," Phys. Rev. **44**, 423 (1933).

[7] Langmuir, I. R. and Taylor, J. B., "Vapor pressure of cesium by the positive ion method," Phys. Rev. **52**, 753 (1937).

[8] Forrester, A. T. and Speiser, R. C., "Cesium-ion propulsion," Astronautics **4**, 34 (October 1959).

[9] Taylor, L. H., "Adsorption of cesium on polycrystalline refractory metals," Surface Sci. **2**, 183 (1964).

[10] LaChance, M., Kuskevics, G., and Thompson, B., Electro-Optical Systems, Inc. EOS Rept. 3720-Final (May 1964).